

Three-dimensionality effects in flow around two tandem cylinders

By GEORGIOS V. PAPAIOANNOU¹, DICK K. P. YUE^{1†},
MICHAEL S. TRIANTAFYLLOU¹
AND GEORGE E. KARNIADAKIS²

¹Department of Mechanical Engineering, Massachusetts Institute of Technology, Cambridge, MA 02139, USA

²Division of Applied Mathematics, Brown University, Providence, RI 02912, USA

(Received 4 November 2004 and in revised form 8 December 2005)

The flow around two stationary cylinders in tandem arrangement at the laminar and early turbulent regime, ($Re = 10^2 - 10^3$), is studied using two- and three-dimensional direct numerical simulations. A range of spacings between the cylinders from 1.1 to 5.0 diameters is considered with emphasis on identifying the effects of three-dimensionality and cylinder spacing as well as their coupling. To achieve this, we compare the two-dimensional with corresponding three-dimensional results as well as the tandem cylinder system results with those of a single cylinder. The critical spacing for vortex formation and shedding in the gap region depends on the Reynolds number. This dependence is associated with the formation length and base pressure suction variations of a single cylinder with Reynolds number. This association is useful in explaining some of the discrepancies between the two-dimensional and three-dimensional results. A major effect of three-dimensionality is in the exact value of the critical spacing, resulting in deviations from the two-dimensional predictions for the vorticity fields, the forces on the downstream cylinder, and the shedding frequency of the tandem system. Two-dimensional simulations under-predict the critical spacing, leading to erroneous results for the forces and shedding frequencies over a range of spacings where the flow is qualitatively different. To quantify the three-dimensional effects we first employ enstrophy, decomposed into a primary and a secondary component. The primary component involves the vorticity parallel to the cylinder axis, while the secondary component incorporates the streamwise and transverse components of the vorticity vector. Comparison with the single cylinder case reveals that the presence of the downstream cylinder at spacings lower than the critical value has a stabilizing effect on both the primary and secondary enstrophy. Systematic quantification of three-dimensionality involves finding measures for the intensity of the spanwise fluctuations of the forces. This also verifies the stabilization scenario, suggesting that when the second cylinder is placed at a distance smaller than the critical one, three-dimensional effects are suppressed compared to the single-cylinder case. However, when the spacing exceeds the critical value, the upstream cylinder tends to behave like a single cylinder, but three-dimensionality in the flow generally increases.

1. Introduction

In many engineering applications, flow past cylinders in tandem or in an array is present; for example, in heat exchanger tubes, tension-leg offshore platforms, and

† Author to whom correspondence should be addressed: yue@mit.edu.

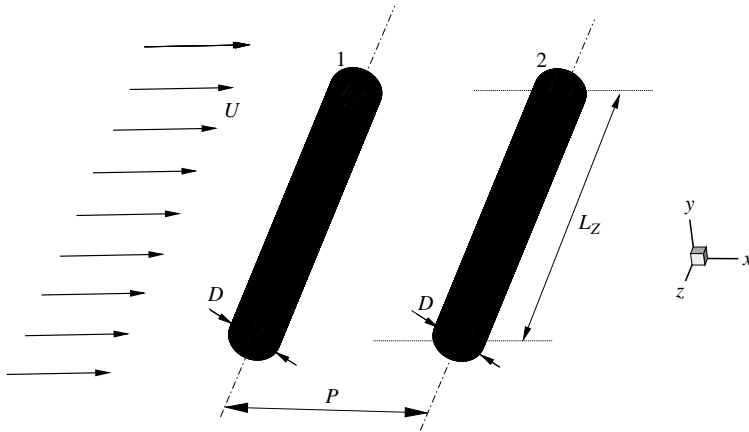


FIGURE 1. Tandem cylinders configuration. P , cylinder spacing; D , cylinder diameter; U_∞ , free-stream velocity; L_z , length of periodic domain in the z -direction.

adjacent tall buildings. Many geometric configurations can result, depending on the distance between the cylinders and their angle relative to the free stream. The present work focuses on flow past a tandem arrangement of two rigid stationary cylinders, i.e. when the axes of the two cylinders are on a plane parallel to the free-stream velocity vector, as shown in figure 1. Side-by-side and staggered arrangements, and flow-induced vibrations will not be discussed in this paper.

One of the earliest efforts to categorize the basic interference flow regimes was that of Zdravkovich (1987). The interference of two cylinders in tandem belonged to a regime that Zdravkovich identified as *wake interference*. According to his definition, wake interference occurs when one cylinder is near to or submerged into the wake of the other. The wake interference regime was subdivided into four major regimes. In the first regime, the cylinders are in such close proximity that the shear layer separating from the upstream cylinder rolls up after the downstream and forms a single wake; this is the *single slender-body regime*. In the second regime, there is a range of spacings for which the shear layers separating from the upstream cylinder reattach on the downstream, defining the reattachment regime. Depending on the way and location where they reattach, this regime can be categorized as *alternating* and *quasi-steady reattachment*. In the third regime, an *unstable* subregion was identified where vortex shedding behind the front cylinder persists for some time and then is intermittently suppressed and replaced by the reattachment flow regime. Finally, in the fourth regime, when the cylinders are sufficiently far apart, two separate vortex streets are formed.

Oka, Kostic & Sikmanovic (1972) measured vortex-shedding frequencies for Reynolds number $Re = 5.1 \times 10^3 - 8.8 \times 10^3$. They did not observe jump in the shedding frequency (Strouhal number St), associated with vortex shedding in the gap region, until the spacing exceeded 3.8 diameters ($P/D \geq 3.8$). Tanida, Okajima & Watanabe (1973) found that the sudden increase in St occurred at $P/D = 3.0$ for $Re = 3.4 \times 10^3$. Igarashi (1981) studied flow characteristics around two tandem cylinders in the Re range of $8.7 \times 10^3 - 5.2 \times 10^4$. He found a critical spacing for frequency jump at $P/D = 3.53$. Okajima (1979) conducted measurements at relatively high Reynolds numbers and found the critical spacing at $P/D = 3.8$ for $Re = 1.7 \times 10^5$ and $Re = 2.5 \times 10^5$. Sumner, Price & Paidoussis (1999) used particle image velocimetry (PIV) to study the temporal and spatial development of the impulsively started flow

around two stationary tandem cylinders at distances 1.0–3.0 diameters and Reynolds numbers in the range 1200–3800. They were able to quantify the location and characteristics of the recirculation zone and provide the time evolutions of primary eddy circulation, area, centre location, and length from base of cylinder. Xu & Zhou (2004) used hot wires in the wake of each cylinder to measure the Strouhal number of two inline cylinders at $Re = 800$ to 4.2×10^4 and spacings $P/D = 1$ to 15. For $Re = 1400$ they calculated a critical spacing $P/D = 4.5$. At $Re = 8500$, they found a critical spacing $P/D = 4.0$ while for $Re = 42\,000$ the critical spacing was $P/D = 3.0$. These results deviate from those previously reported by Tanida *et al.* (1973), Okajima (1979), Igarashi (1981) and others, but agree with the results reported by Ljungkrona, Norberg & Sunden (1991). They attributed the deviations from other authors to different aspect ratio and free-stream turbulence.

Apart from the above experimental studies, the few available numerical ones are two-dimensional. Although a single cylinder is a simple geometry, two of them create geometrical complexity, which is difficult to handle efficiently by structured grid methods. Slaouti & Stansby (1992) employed a random vortex method, enhanced by a vortex in cell scheme on overlapping grids, to study the laminar flow around two cylinders at $Re = 200$. The results of this study showed many of the features observed experimentally. However, the calculation of forces was not very accurate, and frequency analysis for spacings less than the critical for generation of shedding in the gap region presented difficulties. Meneghini *et al.* (2001) used a finite-element method on an unstructured mesh to solve the flow around two cylinders in tandem and staggered arrangements. The simulations in this case were also two-dimensional, and were conducted at $Re = 200$. Mittal, Kumar & Raghuvanshi (1997) used a finite-element method stabilized by the streamwise upwind Petrov–Galerkin (SUPG) and pressure stabilizing Petrov–Galerkin (PSPG) techniques. The flows examined were at $Re = 10^2$ and $Re = 10^3$, and the two tandem arrangements included in their work were for spacings $P/D = 2.5$ and $P/D = 5.0$. For the spacing $P/D = 2.5$, they observed that while at $Re = 10^2$ there was no distinct vortex shedding behind the upstream cylinder, for $Re = 10^3$ there was. They also noted a reduction in the Strouhal number compared to the single cylinder case for the same Re . For the $Re = 10^3$ case, they found that although the near wake was temporally periodic, the far wake was not. Jester & Kallinderis (2003) used a second-order SUPG and dynamic meshing to solve efficiently the two-dimensional flow on a large number of different two-cylinder configurations. Reynolds numbers of 80 and 1000 were considered, and good qualitative and quantitative comparisons with published experimental data were claimed. They were able to reproduce the hysteresis effect first observed experimentally in the work of Zdravkovich (1984). This hysteresis produces an overlap of the reattachment and binary-vortex regimes for a range of spacings, although only one flow regime exists at a time. In this range of spacings, there is reattachment if the cylinder was displaced there from smaller spacings, while there is binary-vortex shedding if it was displaced from larger spacings. In Papaioannou (2003) two cases of hysteresis are demonstrated in the context of two-dimensional numerical simulations starting from different initial conditions. When, for a given spacing and Reynolds number, the flow field corresponding to the solution of lower Reynolds number was used as initial condition, reattachment was preserved. On the other hand, when the initial condition for that spacing was the corresponding flow field at a higher Reynolds number for which the flow was in binary-vortex regime, the flow remained in that regime. This was observed only for a few of the tested spacings, for those that correspond to the regime-overlapping region of spacings.

In the studies mentioned so far, the focus has been on how the spacing between the two tandem cylinders influences the forces and the flow structure as seen by flow visualization of the vorticity component parallel to the cylinders' axes. Three-dimensional effects have not been examined. There are several studies, however, on the three-dimensionality of a single cylinder. Those studies have shown that the development of a spanwise instability of the shed vortices is the onset of three-dimensionality in the wake. An elaborate description of the development of three-dimensionality in the wake of a single cylinder and the different Reynolds number regimes, along with extensive literature references on the topic, is provided by Williamson (1996). The mutual effects between three-dimensionality and cylinder spacing have not been examined in the past.

In the present work, we use direct numerical simulations to gain some insights into those effects at the lower subcritical regime. Specifically, we investigate how three-dimensional predictions of forces and Strouhal frequencies on tandem cylinders deviate from two-dimensional predictions, and examine the reasons for such discrepancies. We compare the primary vorticity flow-field predictions of two- and three-dimensional simulations at corresponding Re . We also study how the presence of a second cylinder and its distance from the first changes the three-dimensionality of the wake. To achieve these objectives we employ both a two-dimensional numerical scheme and a three-dimensional scheme with periodicity imposed in the direction of the cylinders' spans. Both schemes are based on the spectral/hp element method. A series of numerical experiments were performed. For the two-dimensional simulations, the spacing was systematically varied for $Re = 160$ and $Re = 500$. The first Reynolds number was chosen to be just below the onset of three-dimensionality for the single-cylinder case. The second was chosen to be in a regime where three-dimensionality is well developed for the single cylinder with relatively strong streamwise streaks of vorticity (Williamson 1988). Additionally, to track the critical spacing variation with Re , selected spacings around the expected critical spacing were examined at $Re = \{100, 200, 250, 300, 350\}$. For the three-dimensional simulations, the spacing was systematically varied for Reynolds numbers 500 and 1000, where it is known that for a single cylinder the wake has developed considerable three-dimensionality.

This paper is organized as follows. In §2, we provide a brief description of the solution method, both in two- and three-dimensions. In §3, we present the results for the forces and shedding frequencies, explain their variation with cylinder spacing (P/D), and compare between two- and three-dimensional results. In §4, we study the three-dimensional effects on the critical spacing and how the latter varies with the Reynolds number. In §5, we study the way cylinder spacing affects three-dimensionality. Initially, this is done by flow visualization of cases corresponding to the different flow regimes, and subsequently by employing different ways to quantify three-dimensional effects and measure their variation with cylinder spacing. Finally, we conclude with a brief summary. In the Appendix we demonstrate the convergence of selected two- and three-dimensional simulations.

2. Method and formulation

We solve the incompressible Navier–Stokes equations with the following boundary conditions: on the cylinder surface the no-slip condition is prescribed; the infinite domain is truncated and represented by a rectangular domain; a Neumann boundary condition is used at the outflow, imposing zero velocity gradient normal to that boundary (streamwise direction); and the free-stream velocity is prescribed on all

other sides. For the initial condition, we used the solution of the immediately lower available Reynolds number for every given spacing. If that was not available, the free-stream velocity was also used as the initial condition. The equations are normalized by the cylinder's diameter D , the free-stream velocity U_∞ , and the water density which is assumed constant throughout the fluid. We will highlight next the basic elements of the method used to solve the incompressible Navier–Stokes equations. Convergence results for two- and three-dimensions can be found in §A.2.

2.1. Two dimensions

We followed a spectral/hp element approach based on hybrid unstructured meshing (see Warburton 1998). The mesh is referred to as hybrid when it contains both triangular and quadrilateral elements. In the context of spectral/hp elements, increasing the resolution can be achieved by either decreasing the elements' size (h-refinement) or by increasing the order of the polynomials used for a given mesh (p-refinement). The second way is much easier as it does not require remeshing. Generalized tensor products of Jacobi polynomials of mixed weights are used for the trial bases, as discussed in detail in Karniadakis & Sherwin (1999). Each element can accommodate variable spectral order. This is accomplished by hierarchical arrangement of the trial bases in terms of vertex, boundary and bubble modes, and matching of the vertex and boundary modes, so that C^0 continuity is ensured, as required in the Galerkin formulation for incompressible flow. This approach makes it possible to use the same mesh discretization to solve for the different Reynolds numbers considered, just by changing the polynomial order p .

The equations of motion are discretized in time using the high-order fractional-step scheme proposed by Karniadakis, Israeli & Orszag (1991). The first stage of each time step adds the contributions of the nonlinear terms ($u_j u_{i,j}$) to the velocity field. Those contributions are computed explicitly using a stiffly stable integration scheme of order J :

$$\frac{u_i^{n+1/3} - \sum_{q=0}^{J-1} \alpha_q u_i^{n-q}}{\Delta t} = \sum_{q=0}^{J-1} \beta_q [-u_j u_{i,j}]^{n-q}, \tag{2.1}$$

where α_q and β_q are the coefficients for stiffly stable integration. We use second-order-accurate time stepping ($J = 2$).

The next stage adds the contribution of the pressure gradient to the velocity field:

$$\frac{u_i^{n+2/3} - u_i^{n+1/3}}{\Delta t} = -P_{i,i}. \tag{2.2}$$

Continuity is enforced at this sub-step requiring $u_{i,i}^{n+2/3} = 0$. This leads to a Poisson equation for the pressure:

$$P_{,ii}^{n+2/3} = \Delta t^{-1} u_{i,i}^{n+1/3}, \tag{2.3}$$

solved along with a consistent Neumann boundary condition derived from the normal component of the momentum equation:

$$p_{,i} n_i = n_i \left[\sum_{q=0}^{J_e-1} \beta_q (N(u_i^{n-q}) + Re^{-1} L(u_i^{n-q})) \right], \tag{2.4}$$

where $N(u_i) = u_j u_{i,j}$ represents the nonlinear terms of the Navier–Stokes and $L(u_i)$ represents the linear Laplacian terms written in rotational form: $L(u_i) = u_{i,jj}$

$= -\epsilon_{ijk}\epsilon_{klm}u_{m,lj}$. In the final stage, the viscous correction is computed by solving a Helmholtz equation, also enforcing the velocity boundary conditions:

$$\frac{\gamma_0 u_i^{n+1} - u_i^{n+2/3}}{\Delta t} = \frac{u_{i,jj}^{n+1}}{Re}, \quad (2.5)$$

where $\gamma_0 = \sum_{q=0}^{J-1} \alpha_q$ is the backwards differentiation coefficient in the stiffly stable scheme. The total force can be simply calculated by numerical integration of the calculated pressure and viscous stress terms:

$$F_i(t) = \oint [-p n_i + Re^{-1}(u_{i,j} + u_{j,i})u_j], \quad (2.6)$$

where n_i is the normal vector.

This method has several advantages. One of them is the high accuracy due to the convergence characteristics of the spectral/hp elements. Another advantage is the efficiency achieved by the explicit treatment of the nonlinear terms and the fact that the other two sub-steps are the well understood and efficiently solved Helmholtz equations.

2.2. Three dimensions

To solve the problem in three dimensions, additional boundary conditions have to be prescribed. Periodic boundary conditions were used at the spanwise truncation of the mesh to avoid phenomena such as contamination by end-effects, known from experimental studies to cause disturbances, especially when studying the spanwise instability of the wake. For the present problem where the cylinders are rigid and stationary, efficiency is improved by using a hybrid scheme using Fourier collocation in the spanwise direction (z) and Jacobi–Galerkin formulation on planes perpendicular to the cylinder (x, y). To reduce aliasing errors a 3/2 rule is employed. Details of this scheme can be found in Henderson & Karniadakis (1995). To use Fourier expansions in the z -direction, the assumption that all variables are periodic in this direction has been made:

$$u_i(x_1, x_2, x_3; t) = \sum_{m=0}^{M-1} [u_i]^m(x_1, x_2; t) \exp(i\kappa m x_3), \quad (2.7)$$

where κ is the x_3 -direction (or z -) wavenumber defined as $\kappa = 2\pi/L_z$. A similar splitting scheme as in the two-dimensional formulation is used for the transformed Navier–Stokes equations. The choice of the spanwise length L_z of the domain was based on efficiency and accuracy considerations. On those grounds and from past experience, a spanwise length of $L_z = 3\pi$ was considered sufficient for the numerical experiments presented in this work.

This method has several advantages. First, the use of Fourier collocation in the z -direction enables us to use the same two-dimensional meshes we used for the two-dimensional simulations for corresponding spacings. Secondly, it scales almost perfectly for parallel computations. Specifically, the assignment of different modes to different processors reduces communications among the processors and increases the efficiency and scalability for parallel computations. Fourier expansions are an optimal base for periodic functions and the fast Fourier transform (FFT) is computationally efficient.

3. Calculation of shedding frequencies and cylinder forces

3.1. Shedding-frequency variation with cylinder spacing

Before we start analysing the tandem cylinders, we provide a result that establishes the validity of our calculations for a single cylinder. Figure 2 shows a comparison

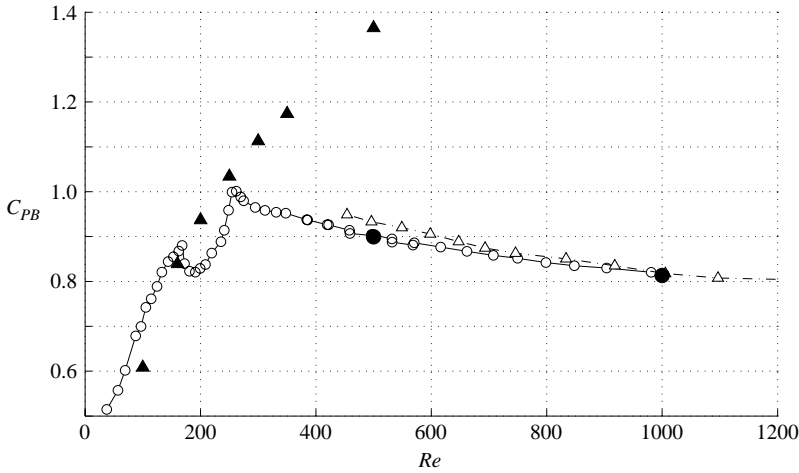


FIGURE 2. Comparison among different studies of the base pressure coefficient ($-C_{PB}$) of a single cylinder for different Reynolds numbers. \circ , Williamson & Roshko 1990; Δ , Norberg (1994); \bullet , present results, three dimensions; \blacktriangle , present results, two dimensions.

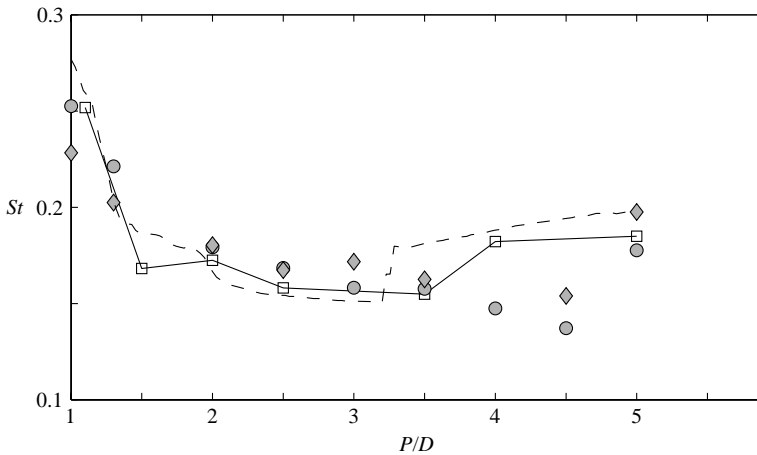


FIGURE 3. Comparison of Strouhal frequency calculated in the present study with published experimental results. $-\square-$, current CFD results for $Re = 10^3$; \circ , experiments by Xu & Zhou (2004) at $Re = 1.3 \times 10^3$; \diamond , experiments by Xu & Zhou (2004) at $Re = 2.9 \times 10^3$; $---$, experiments by Igarashi (1981) at $Re = 2.2 \times 10^4$.

of the variations in base pressure suction with the Reynolds number, between our numerical data (two- and three-dimensional) and published experimental studies. The base pressure suction is sensitive to the near-wake topology and it serves as a good measure for comparisons. The three-dimensional predictions are in agreement with the experimental results by Norberg (1994), as well as those by Williamson & Roshko (1990).

In figure 3 we compare our shedding frequency results based on the three-dimensional calculation for $Re = 10^3$, with experimental data. There is relatively good agreement with most of the experimental data displayed for a wide range of spacings. However, the critical spacing predicted by Xu & Zhou (2004) is quite high, resulting in a disparity at spacings $P/D = 4-4.5$. Figure 4(a) shows a comparison of the shedding frequencies between two- and three-dimensions for $Re = 500$. The frequencies

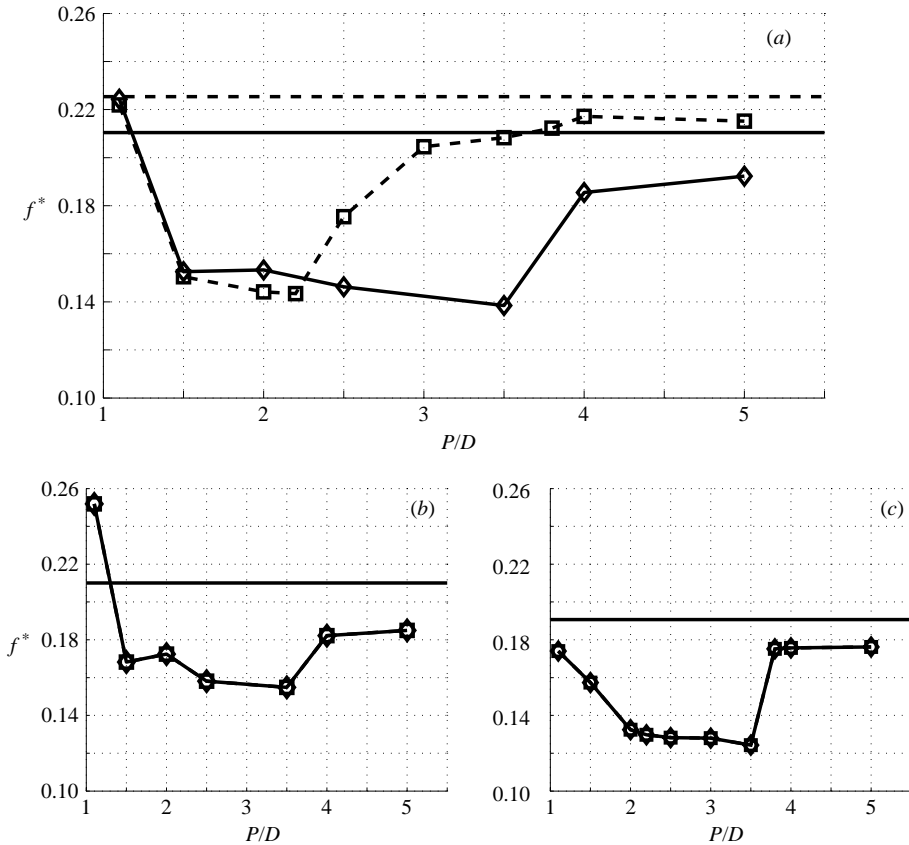


FIGURE 4. Frequency response based on C_L signal for each cylinder. (a) Comparison between two- and three-dimensional for $Re = 500$. —◇—, Tandem three-dimensional; - -□- -, Tandem two-dimensional; —, stand-alone cylinder three-dimensional; - - -, stand-alone cylinder two-dimensional. (b) $Re = 10^3$, three-dimensional: C_L frequency responses are identical for upstream and downstream cylinder. —◇—, Upstream cylinder; - -□- -, downstream cylinder; —, stand-alone cylinder. (c) $Re = 160$, two-dimensional: C_L frequency responses are identical for upstream and downstream cylinder. —◇—, Upstream cylinder; - -□- -, downstream cylinder; —, stand-alone cylinder.

presented in figure 4 are based on spectral analysis of the lift force time series for each cylinder. The discrepancy is significant for a range of spacings between 2.5 and 4.0 diameters. As will be discussed in detail later, this is due to the under-prediction of the critical spacing by the two-dimensional calculations. It is also found that the frequency of the force response is identical on both the upstream and downstream cylinder for each of the spacings examined both in two- and three-dimensions as illustrated in figure 4(b, c).

Spectral analysis was performed on both components of the force. As expected from single-cylinder results, the frequency response of the streamwise component of the force (drag) was found at double the frequency of the vertical component (lift). For very small spacings (proximity regime), the system sheds as a single body, at a frequency close to that of a single cylinder, perhaps not surprisingly, since the frequency is largely determined by the lateral distance of the emanating shear layers. Subsequently, there is a sudden decrease in the shedding frequency as the flow passes

Work	Re	P/D	$\overline{C_D}^{-1}$	$\overline{C_D}^{-2}$	St	Method
Ljungkrona <i>et al.</i> (1991)	100	3.0	1.11	-0.03	0.110	Control volume, SIMPLE
Present work	100	3.0	1.16	0.00	0.116	Spectral/hp, fractional step
Ljungkrona <i>et al.</i> (1991)	100	4.0	1.28	0.71	0.148	Control volume, SIMPLE
Present work	100	4.0	1.31	0.75	0.152	Spectral/hp, fractional step
Meneghini <i>et al.</i> (2001)	200	3.0	1.00	-0.08	0.125	Galerkin FEM, fractional step
Slaouti & Stansby (1992)	200	3.0	0.87	-0.16	0.128	Random vortex
Present work	200	3.0	1.02	-0.12	0.128	Spectral/hp, fractional step
Slaouti & Stansby (1992)	200	3.5	0.85	-0.18	0.12	Random vortex
Present work	200	3.5	1.27	0.40	0.174	Spectral/hp, fractional step
Jester & Kallinderis (2003)	10^3	3.0	1.42	0.16	NA	FEM, SUPG stabilization
Present work	10^3	3.0	1.44	0.13	0.222	Spectral/hp, fractional step
Jester & Kallinderis (2003)	10^3	3.5	1.43	0.16	NA	FEM, SUPG stabilization
Present work	10^3	3.5	1.45	0.12	0.224	Spectral/hp, fractional step

TABLE 1. Comparison of $\overline{C_D}$ and St among various two-dimensional numerical studies for corresponding Reynolds numbers and spacings. (NA denotes 'not available'.)

from the proximity to the reattachment regime. This abrupt change could relate to the bi-stable behaviour of the flow in the transition between these two regimes observed by Xu & Zhou (2004). In the reattachment regime, the shedding is suppressed in the gap region and occurs after the downstream cylinder. The oncoming velocity on the second cylinder is reduced owing to shielding by the upstream cylinder, and in general there is less vorticity generation in both cylinders. The shedding frequency reaches a minimum just before the critical spacing. For spacings larger than the critical value, the shedding frequency is increasing towards that of a single cylinder. As the separation distance increases past the critical spacing and vortex shedding from the upstream cylinder occurs in the gap region, the effect of the downstream cylinder on the upstream one is drastically diminished, allowing it to shed as if it were standing alone. The downstream cylinder, on the other hand, is synchronizing its shedding with the oncoming vortices, forming a binary vortex wake. This results in only one detectable frequency on the force time-history of the downstream cylinder as well as on other time-histories of fixed points in the wake.

3.2. Force calculations

At this stage, it is useful to present some results that establish the validity of our force calculations. Because experimental data on the forces are not available for very low Reynolds numbers, we compare some of the two-dimensional results we obtained with the corresponding cases in other published numerical studies. Table 1 includes a quantitative comparison of $\overline{C_D}$ as well as shedding frequency. There is good agreement between our results and corresponding results from Meneghini *et al.* (2001), Jester & Kallinderis (2003), and Sharman *et al.* (2005). In figure 5, the three-dimensional calculations of $\overline{C_D}$ at $Re = 10^3$ are plotted, along with some experimental data in the subcritical regime, yielding a satisfactory comparison. The difference in Reynolds number among the cases compared justifies the small differences shown in the figure and are consistent with physical intuition, i.e. the differences in C_D are larger for the downstream cylinder, and the higher Reynolds number yields a lower C_D for the upstream cylinder.

For the entire range of spacings examined, $\overline{C_D}$ of each of the two cylinders remains smaller than that of a single cylinder standing alone at the same Re flow. In fact,

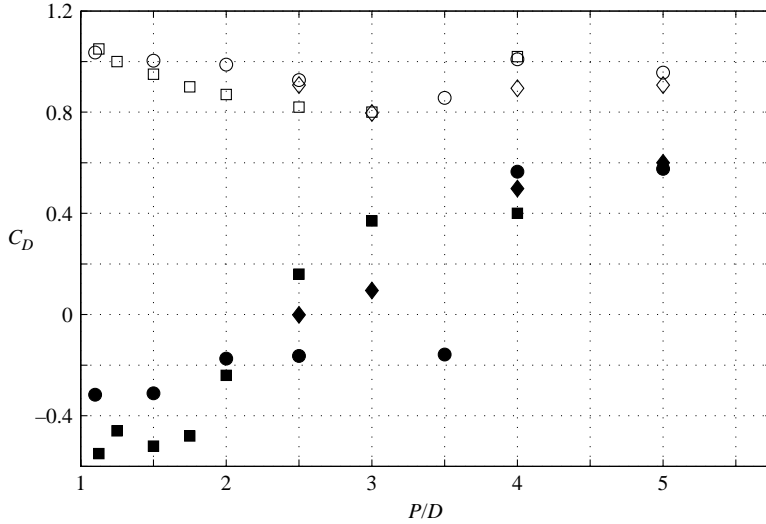


FIGURE 5. Comparison of C_D prediction with experimental data. \circ , current CFD results for $Re = 10^3$; \square , experiments by Tanida *et al.* (1973) at $Re = 3.2 \times 10^4$; \diamond , experiments by Tanida *et al.* (1973) at $Re = 3.4 \times 10^3$. Filled symbols correspond to the downstream cylinder while open symbols correspond to the upstream one.

the downstream cylinder is experiencing negative drag. Furthermore, for spacings smaller than the critical spacing, the mean of the total force on the tandem system is less than that of the single-cylinder case. In the proximity regime, the drag on the upstream cylinder is almost identical to that of a single cylinder at corresponding Re . There are no abrupt changes in the $\overline{C_D}$ during the transition from proximity to reattachment regime, such as those observed on the shedding frequency that we related to the bi-stable character of the flow discussed by Xu & Zhou (2004). In the reattachment regime, $\overline{C_D}$ of the upstream cylinder is decreasing with increasing spacing. At the critical spacing there is a jump in the values of the forces. This jump is more pronounced on the drag force of the downstream cylinder, which changes sign and from negative it becomes positive. The forces on the upstream cylinder tend to those of a single cylinder with increasing spacing after the critical value.

The variation of the drag coefficient with spacing for a given Re was found to follow the variations of the difference between the base pressure (C_{PB}) and the front stagnation-point pressure (C_{PG}) coefficients. It should be clarified that those points are defined by their 'nominal' position on each cylinder. Thus, for each cylinder, front stagnation and base points are defined as the upstream and downstream anti-diametric points parallel to the free stream. For each cylinder and each Reynolds number examined we formed a linear transformation:

$$\overline{C_{Di}} = \alpha(C_{PGi} - C_{PBi}) + \beta. \quad (3.1)$$

The coefficients α and β were found by solving a least-squares problem of all available spacings, separately for each body and each Reynolds number. This procedure gave a good fit of the drag coefficients for both two-dimensional and three-dimensional results (as seen in figure 6). Such transformation was found to perform well both in two and three dimensions. The observation may have limited practical value because α and β are different for each Re and each cylinder. However, its importance seems to lie in the fact that the variation of the forces with spacing can be captured by

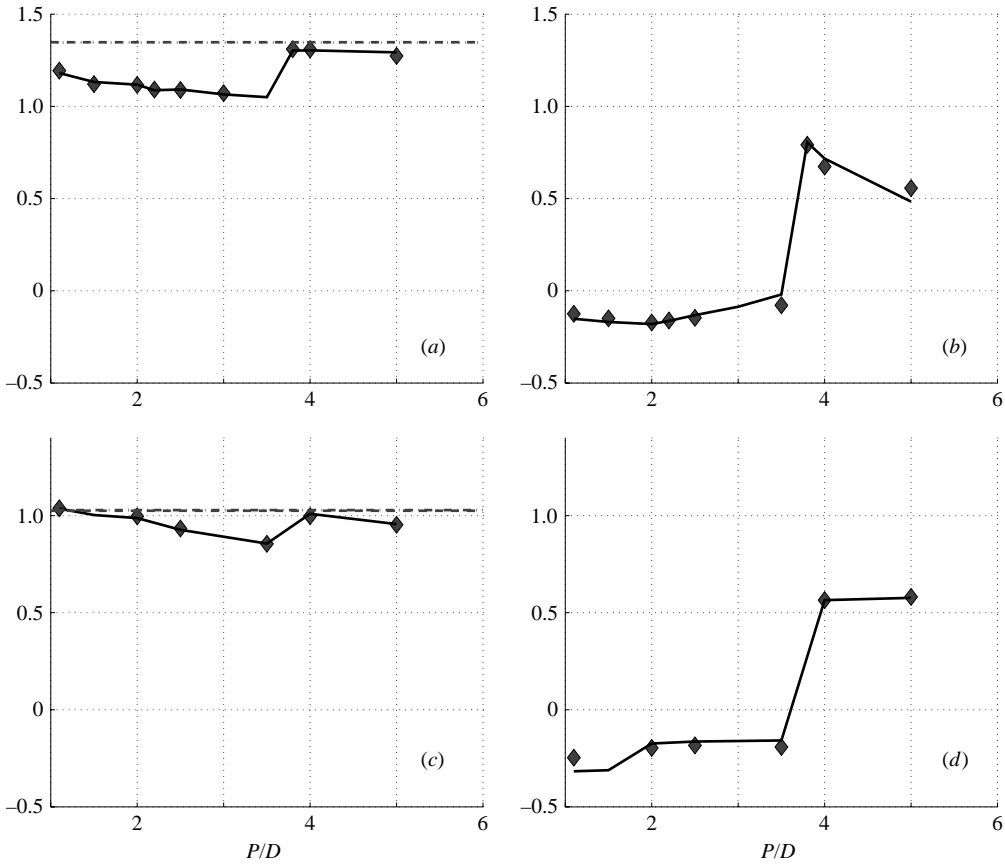


FIGURE 6. Comparison of C_D with linear mapping $\alpha(C_{PG} - C_{PB}) + \beta$. —, C_D for tandem system; \blacklozenge , linear mapping for tandem system; - · -, C_D for single stand-alone (S-A) cylinder; ----, linear mapping for S-A cylinder; (a) two-dimensional: $Re = 160$ upstream cylinder and S-A cylinder; $(\alpha, \beta) = (0.77, -0.16)$. (b) two-dimensional: $Re = 160$ downstream cylinder; $(\alpha, \beta) = (1.01, 0.10)$. (c) three-dimensional: $Re = 10^3$ upstream cylinder and S-A cylinder; $(\alpha, \beta) = (0.67, -0.23)$. (d) three-dimensional: $Re = 10^3$ downstream cylinder; $(\alpha, \beta) = (0.80, 0.00)$.

the variation of the pressures on those two points. For instance, the decrease of the $\overline{C_D}$ with increasing spacing in the reattachment regime can be attributed to a decrease in the base pressure suction ($-C_{PB}$) owing to a shift in the locus of the recirculation region immediately after the upstream cylinder. Notice also that with the same coefficients, the transformation fits the forces well for the reattachment as well as the binary-vortex regime. The success of the same transformation in both regimes can be attributed to the sensitivity of C_{PB} in the near wake vortex formation behind each cylinder and the ability of C_{PG} to account for the shielding effect on the downstream cylinder.

3.3. Deviations between two- and three-dimensional forces and shedding frequency calculations

As seen in §§ 3.1 and 3.2, near the spacing where transition occurs from reattachment to binary vortex-shedding regime, there are abrupt changes in the forces as well as the shedding frequency. For $Re = 500$ we can directly compare the two-dimensional

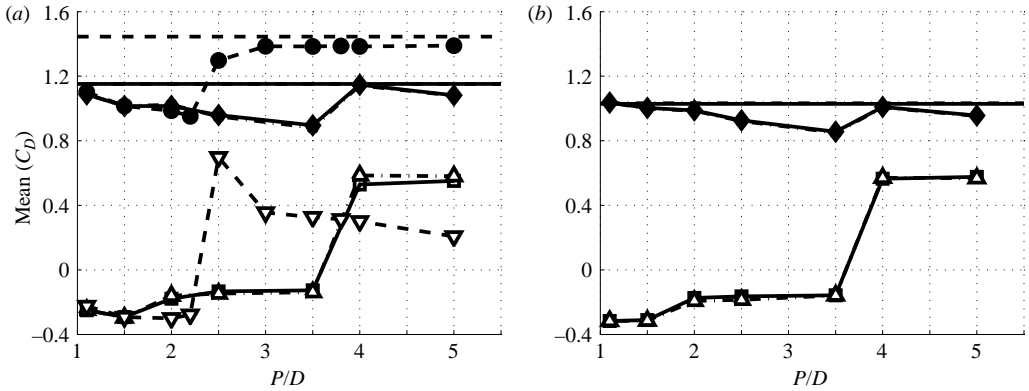


FIGURE 7. Time averages of spanwise mean and maximum sectional drag coefficient of upstream and downstream cylinders along with comparison in two-dimensions. —◇—, three-dimensional average, Cylinder-1; —□—, three-dimensional average, Cylinder-2; -·-·-·-, three-dimensional sectional, Cylinder-1; -·-△-·-·-, three-dimensional sectional, Cylinder-2; -·-●-·-·-, two-dimensional, Cylinder-1; -·-▽-·-·-, two-dimensional, Cylinder-2. (a) $Re = 500$; (b) 1000.

with the three-dimensional results (see figure 7). The results agree quite well for small spacings, i.e. in the proximity and early reattachment regimes. The first minor differences appear on the forces of the downstream cylinder at $P/D = 2.0$, but the comparison is still quite good. Somewhere between $P/D = 2.2$ and $P/D = 2.5$ the two-dimensional predicts transition to binary vortex regime and the forces and frequency increase abruptly. For a relatively wide range of spacings extending from $P/D = 2.2$ to $P/D = 3.5$ the results are completely different quantitatively and qualitatively as well, because the flow is classified differently by the two- and three-dimensional calculations.

After the spacing $P/D = 3.8$, the vortex formation and shedding in the gap region occurred in three-dimensional case as well, and the two- and three-dimensional predictions resume qualitative agreement. However, quantitatively the two-dimensional code over-predicts the C_D of the upstream cylinder and under-predicts that of the downstream, while over-predicting the shedding frequency. This is because the two-dimensional simulation allows for a higher strength of vortices shed by the upstream cylinder, thus creating a stronger low pressure between the two cylinders. Figure 7 also shows that the C_D of a section of the three-dimensional cylinder is quite different from the corresponding two-dimensional cylinder. This indicates that the main reason for the discrepancies between the two- and three-dimensional forces at this Re is the weakening of the strength of the primary shedding in favour of the crossflow component of the vorticity, and not poor spanwise correlation and cancellation due to phase difference.

4. Three-dimensional effect on the critical spacing

As we have already discussed, it is evident that the transition from the reattachment to binary-vortex regime is the cause of abrupt changes to the forces on the cylinders and the general characteristics of the flow. It can also be seen that there is a different prediction of the critical spacing ($(P/D)|_{CR}$) for the $Re = 500$ case by the two- and three-dimensional simulations. In figure 8, we show the variation of the critical spacing with Reynolds number, as predicted by two- and three-dimensional simulations. The

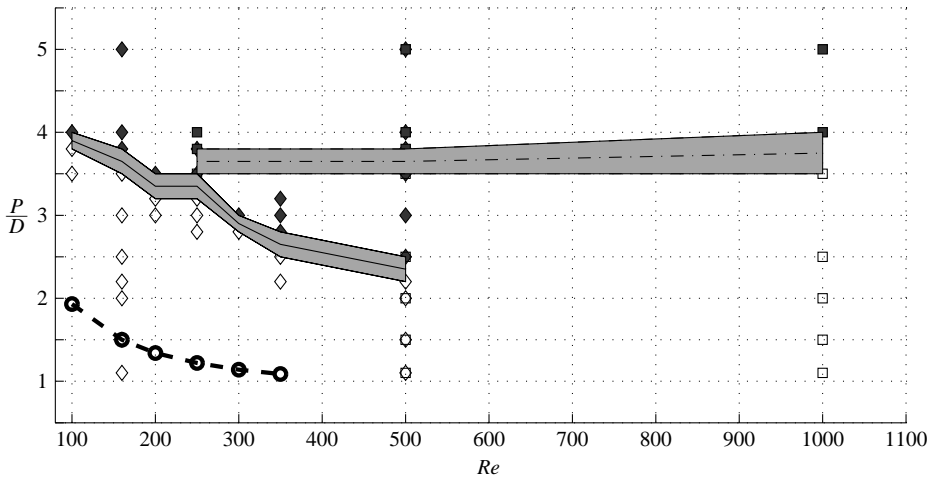


FIGURE 8. Variation of critical spacing with Reynolds number in two- and three-dimensional simulations. \square , three-dimensional reattachment; \diamond , two-dimensional reattachment; \blacksquare , three-dimensional binary vortex; \blacklozenge , two-dimensional binary vortex; —, middle distance between P/D of last reattachment and first binary vortex case of two-dimensional simulations for given Re ; ---, middle distance between P/D of last reattachment and first binary vortex case of three-dimensional simulations for given Re ; - - \circ - -, variation of the recirculation region length for a stand alone (S-A) cylinder with Re (two-dimensional prediction).

same plot also serves as a schematic map of all the cases examined and the regimes to which they were found to belong. The location of the critical spacing for a given Reynolds number is obtained approximately between the last reattachment and first binary-vortex wake case. Because the P/D resolution did not allow a very accurate estimation, the shaded regions of figure 8 represent the range within which the critical spacing lies for each Reynolds number.

We have also plotted the variation of the length of the mean recirculation region behind a single cylinder (L_F^0) as predicted by our two-dimensional calculations. In the present work this was found by calculating the time average field over at least twelve shedding periods after steady states have been achieved, and finding the location of the streamline saddle points. An equivalent result is obtained by finding the intersection of the the x -axis with the zero contour or the maximum root mean square (r.m.s.) of the horizontal velocity. Transferring to logarithmic axes and measuring the slope, we find that in our two-dimensional prediction $L_F^0 \propto Re^{-1/2}$. A similar procedure is applied for the base suction coefficient of a single cylinder obtained by the two-dimensional simulations and shown in figure 2. It was found that $-C_{PB} \propto Re^{1/2}$. This verifies the discovery made by Bearman (1965) that the base suction is very closely inversely proportional to the formation length. It is known that the monotonic decrease of L_F^0 (or equivalently, the monotonic increase of $-C_{PB}$) with Re ceases with the onset of three-dimensionality in the wake. Gerrard (1966) showed that in the turbulent regime, L_F^0 initially grows with Re and reaches a maximum between $Re \approx 2 \times 10^3$ and 5×10^3 , depending on the aspect ratio of the cylinder, but it then decreases for further increasing Re . Norberg (1998) found the local maximum of L_F^0 near $Re = 1.6 \times 10^3$. We assume that the inverse proportionality relation between L_F and $-C_{PB}$ is still valid after the onset of three-dimensionality. Figure 8 shows that the critical spacing is one to two diameters larger than the L_F of a single cylinder at the corresponding

Reynolds number. This suggests that the presence of the downstream cylinder in relative proximity is stabilizing the near-wake region of the upstream.

It can also be inferred from figure 8 that for Re where three-dimensionalities are significant, the two-dimensional simulations under-predict the critical spacing. To explain this we return to the $-C_{PB}$ variation with Reynolds number for a single cylinder. As seen in figure 2, contrary to the two-dimensional prediction, the base pressure suction calculated by the three-dimensional simulation results is reducing very slowly as Re increases from 500 to 1000. Invoking the inverse proportionality assumption between L_F and $-C_{PB}$, as well as the data of Gerrard (1966) and Norberg (1998), we expect L_F^0 to be increasing in the Re range 500 – 1000. Even though a precise relationship between the formation length of a single cylinder and the critical spacing of two tandem cylinders has not been found to exist, their qualitative variation with Re appears consistent in both the two- and three-dimensional simulation results.

5. Stabilizing effect of the downstream cylinder in relative proximity to the upstream

5.1. Vorticity fields

In figures 9 to 12, instantaneous vorticity fields are plotted for visualization and examination of the flow structure. All displayed cases correspond to $Re = 500$. The case $P/D = 1.1$ (figure 9) corresponds to the proximity regime and demonstrates relatively strong spanwise correlation and similarity to the corresponding two-dimensional case. The spacing $P/D = 2.0$ (figure 10) was chosen to compare the two- and three-dimensional results for a reattachment case. Spacing $P/D = 5.0$ (figure 12) illustrates a binary vortex regime case while $P/D = 3.5$ (figure 11) corresponds to a case where the two- and three-dimensional give predictions in different regimes. Comparison of the three-dimensional results for $P/D = 2.0$ and $P/D = 3.5$ cases shows different locations of the reattaching sheets on the downstream cylinder. This is in accordance to the sub-categorization of the reattachment regime to ‘alternating’ and ‘quasi-steady’ by Zdravkovich (1977). For a complete set of flow visualizations for all examined cases (see figure 8), see Papaioannou (2003).

On the left-hand sides of figures 9 to 12, the z -component of the vorticity at four spanwise sections of the cylinder ((a)(i)–(a)(iv)) is compared with the two-dimensional vorticity field corresponding to the same case ((a)(v)). This plot also gives an illustration of the three-dimensionality by noting the difference in the instantaneous vorticity among different spanwise locations. In cases of relatively high three-dimensionality, the phase of primary vortex shedding varies among different spanwise sections, and vorticity components non-parallel to the cylinder’s axis become significant. The spanwise location of the (x, y) -planes is shown by the horizontal lines in parts (b)(i) of figures 9–12. The instantaneous vorticity vector magnitude of the tandem system is plotted at a plane section $y = 0$. In a two-dimensional flow, the vorticity should appear in straight bands parallel to the z -axis. With developing three-dimensionality, those bands lose their uniformity. Originally they become wavy and subsequently they are disrupted from vortex dislocations. Below, the corresponding view for a single cylinder is plotted for comparison of the three-dimensionality between the tandem system at the different regimes and the single cylinder at corresponding Re . Figure 10 shows that the spanwise deviations of the vorticity magnitude in the tandem $P/D = 2.0$ case are less than in the single-cylinder case. Both two- and three-dimensional predictions are in the reattachment regime for this spacing. There is obvious spanwise periodic structure evident in the (x, y) plot with prominent components in the second and fourth modes.

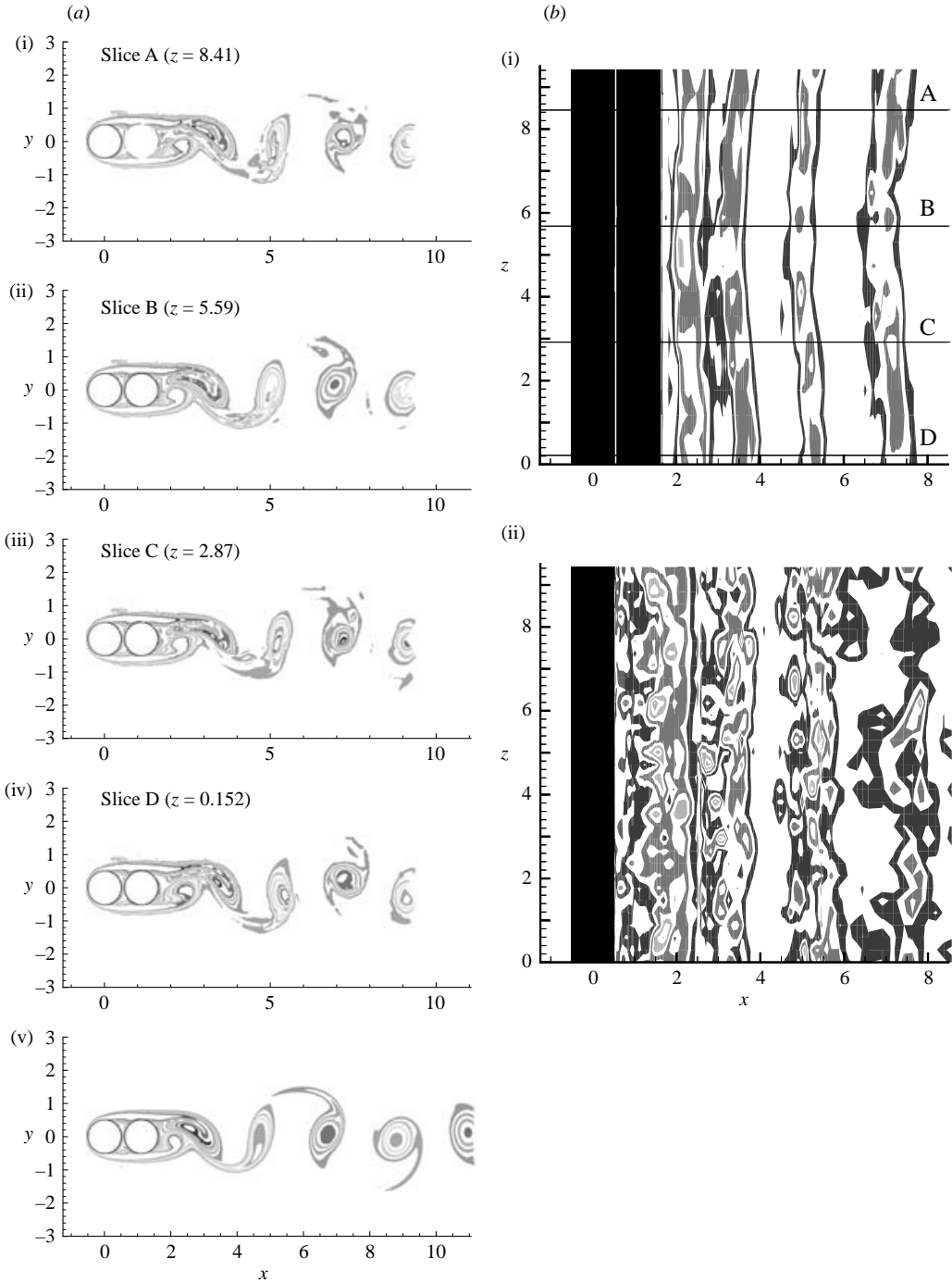


FIGURE 9. Proximity regime case corresponding to spacing $P/D = 1.1$ and $Re = 500$. ((a)(i)–(a)(iv)) show the z -component of the instantaneous vorticity field, on four different (x, y) -planes across the span of the cylinder. Those planes correspond to the horizontal lines of (b)(i) which shows the magnitude of the instantaneous vorticity vector at the (x, z) -plane at $y=0$. The two-dimensional vorticity field is plotted in (a)(v) for comparison with the z -vorticity slices. The vorticity magnitude in the $y=0$ plane of a single cylinder is plotted in (b)(ii) for comparison with the corresponding view for the tandem system.

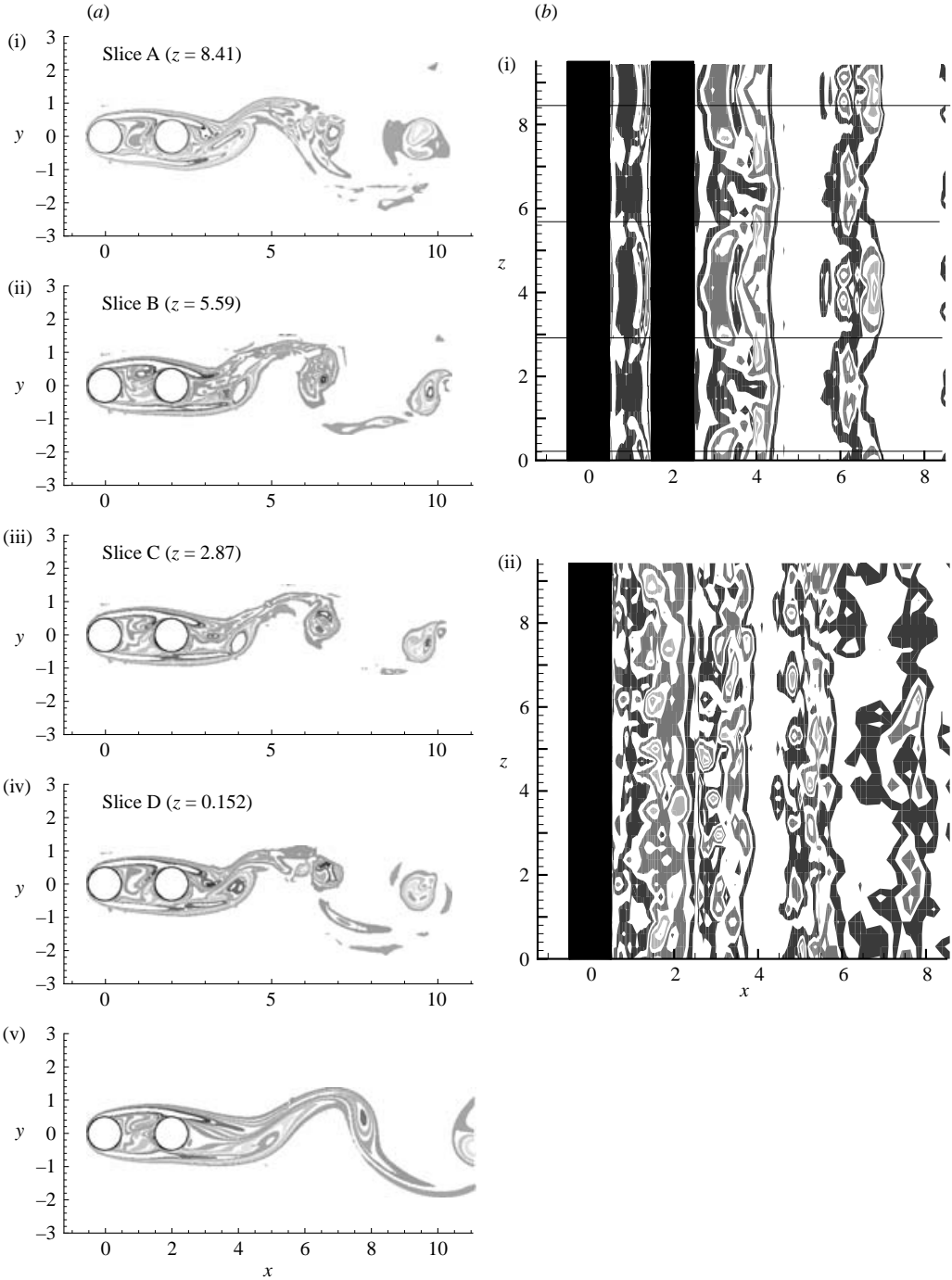


FIGURE 10. *Reattachment regime* case corresponding to spacing $P/D = 2.0$ and $Re = 500$. The vorticity fields are instantaneous and the figure is outlined similarly to figure 9.

There is an indication that the presence of the downstream cylinder is stabilizing the wake in the gap region. The single-cylinder case exhibits more significant three-dimensionality at a distance from the cylinder corresponding to the extent of the gap

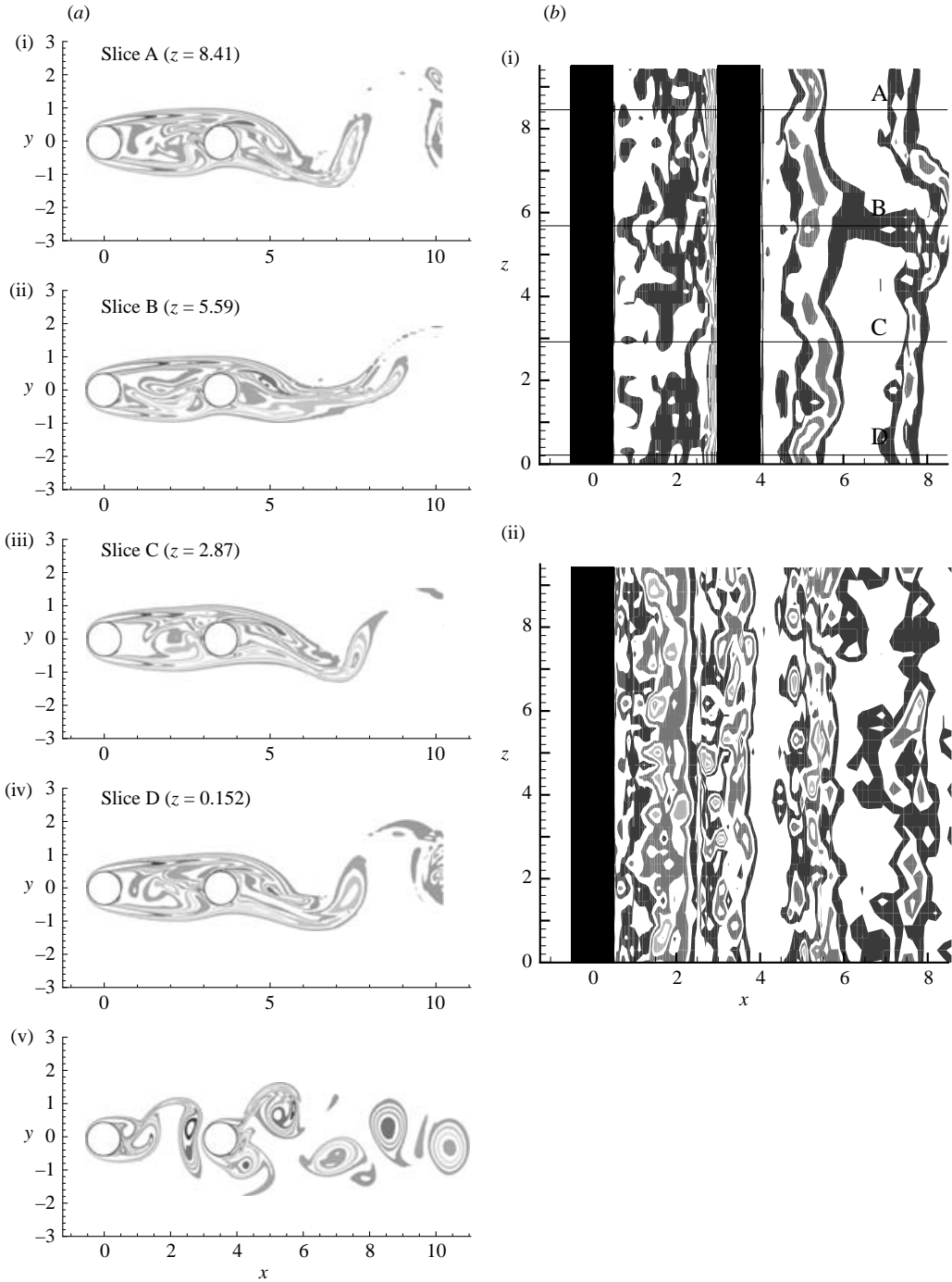


FIGURE 11. Instantaneous vorticity for spacing $P/D = 3.5$ and $Re = 500$. The three-dimensional simulations predict *reattachment* for this case, while the two-dimensional result, (d)(v), predicts vortex shedding in the gap region classifying this case in the *co-shedding* or *binary-vortex* regime.

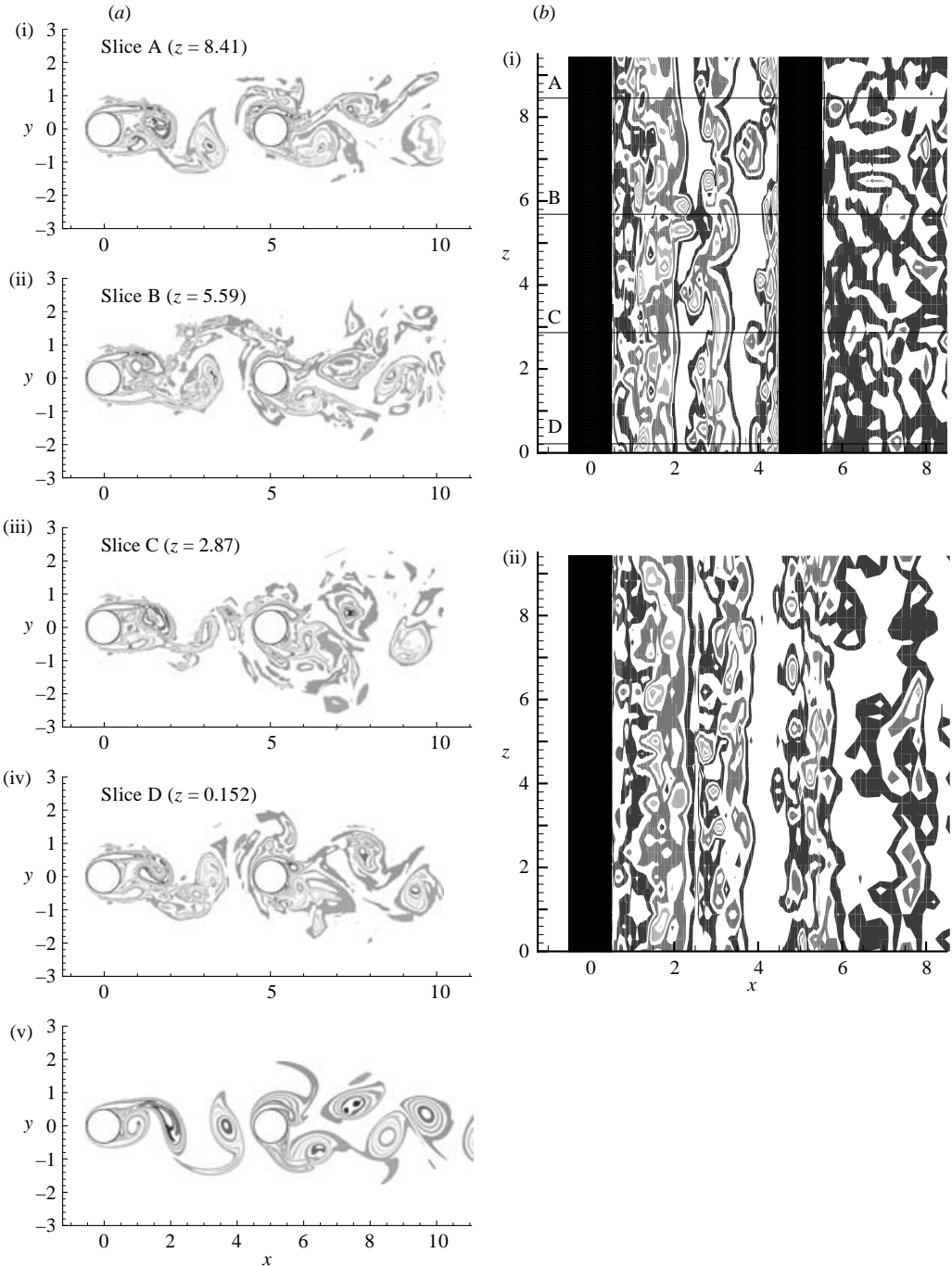


FIGURE 12. *Binary-vortex* or *co-shedding* regime case corresponding to spacing $P/D = 5.0$ and $Re = 500$. Both two- and three-dimensional simulations classify this case in the same regime.

region. This is a consequence of the stabilizing effect it has on the primary vorticity in the gap region where the crossflow vorticity draws energy. Streamwise and spanwise components of the vorticity gain in strength as vorticity is convected downstream

at the expense of spanwise (primary shedding) vorticity. The prevention of vortex roll-up and the formation of a strong vortex core in the gap region suppresses three-dimensionality as well, because at the Re range considered, the development of three-dimensionality comes from an original undulation of primary vorticity and the formation of vortex dislocations on the core of primary vortices. In the reattachment regime, the three-dimensionality in the gap region generally increases with cylinder spacing. For increasing spacing within the reattachment regime, the shear layer that reattached on the front side of the downstream cylinder is drawn into the gap from at least one of the two sides. The case $P/D = 3.5$ (figure 11) shows considerable primary vorticity in the gap region, but it is distinctly different from cases belonging to the binary vortex regime. Apart from the difference in the measured forces on the downstream cylinder, there is a qualitative difference in that the spanwise vorticity in the gap region is drawn from the reattachment site on the downstream cylinder rather than an immediate roll-up of the shear layer emanating from the upstream. This qualitative difference is illustrated in figure 11 by comparison of the three-dimensional sections that indicate reattachment with the two-dimensional result for the same spacing that predicts vortex shedding in the gap region. Past the reattachment regime ($P/D > 3.5$) where vortex shedding occurs in the gap region, the three-dimensionality increases between the cylinders as well as the entire wake, as illustrated in figure 12. The flow in the binary vortex regime exhibits more three-dimensionality than the single-cylinder case.

5.2. Quantification by enstrophy calculation

The *enstrophy* is defined as the variance of the vorticity, i.e.

$$D(t) = \int_{\Omega} \omega_i^2(x_i, t) dV = \int_{\Omega} (\epsilon_{ijk} u_{k,j})^2 dV, \quad (5.1)$$

where tensor notation is employed for compactness in (5.1). The vorticity vector is denoted as ω_i , and the velocity as u_i . The idea is to use the enstrophy integral to quantify the vorticity fields presented and to make the comparisons among different cylinder spacings more meaningful. The mesh handling and merging technology we developed allowed the use of the same outer mesh for all examined spacings, ensuring that the limits of integration of the enstrophy integral are consistent among all examined cases.

At every time step, the whole field is solved for the primitive variables (u_i, p). The enstrophy is calculated directly by numerical differentiation of the calculated velocity, subsequent calculation of the vorticity field, and squaring and integrating. In the three-dimensional calculations, the vorticity is a three component vector. As an alternative way of quantifying three-dimensionality, the *secondary enstrophy* is calculated; it is defined as the total enstrophy based on the streamwise (x) and lateral (y) components of the vorticity, i.e.

$$D_V(t) = \int_{\Omega} (\omega_x^2(x_i, t) + \omega_y^2(x_i, t)) dV. \quad (5.2)$$

This gives the total enstrophy based on components of the vorticity not present in a two-dimensional calculation. Measurement of the total enstrophy and *primary* component of the enstrophy (D_z), and comparison with the corresponding two-dimensional enstrophy calculation can enhance the understanding of how the two- and three-dimensional results differ. Figure 13 shows that for a given Reynolds number, the total enstrophy for spacings lower than the critical is smaller than that of a single

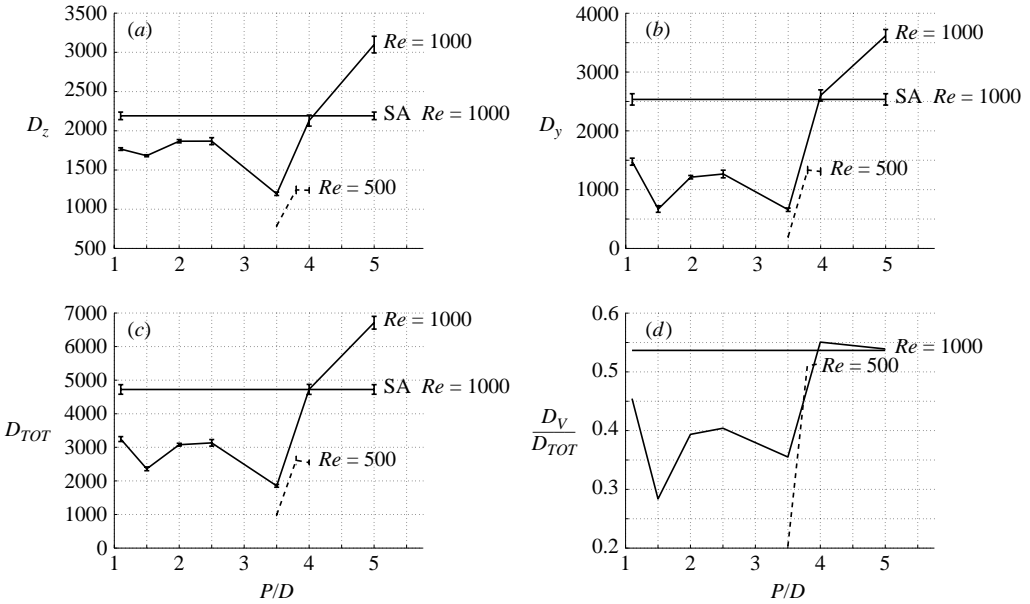


FIGURE 13. Entrophy variations with cylinder spacing and comparison with a single cylinder. (a) Primary entrophy (D_z). (b) Secondary entrophy (D_y). (c) Total entrophy (D_{TOT}). (d) Fraction of primary to total entrophy.

cylinder. The same is true also for the secondary and primary entrophy components. This result is also in support of the wake stabilization scenario suggested earlier.

In the two-dimensional simulations, the secondary entrophy does not exist. The question that arises is how the primary and total entrophy predicted by the three-dimensional simulation compare with those of two-dimensions for a particular spacing and Reynolds number. In figure 14, the question is answered for spacings $P/D = 3.5$ and $P/D = 4.0$. For $P/D = 4.0$, which is past the critical spacing for both the two- and three-dimensional predictions, the total entrophy of the three-dimensional simulation is higher than that of the two-dimensional simulation. The opposite is true for the primary entrophy, where it is clearly over-predicted by two-dimensions. In the case $P/D = 3.5$, the entrophy calculated by the two-dimensional simulations is also greater than the total entrophy of the corresponding three-dimensional result. We should point out, however, that this spacing is classified in the reattachment regime by the three-dimensional result while for the two-dimensional it is already in the binary vortex-shedding regime. As discussed earlier and supported also by figure 13, the entrophy is increasing significantly with inception of vortex shedding in the gap region.

5.3. Spanwise variations

The study of three-dimentionalities proceeds with the analysis of the spanwise and time variations of forces, or the pressure and velocity signals. To make the presentation more clear, we make the following conventions: Spanwise averaging is denoted as $\langle \rangle$:

$$\langle g(z, t) \rangle = \frac{\sum_{i=1}^M g(z_i, t)}{M}, \quad (5.3)$$

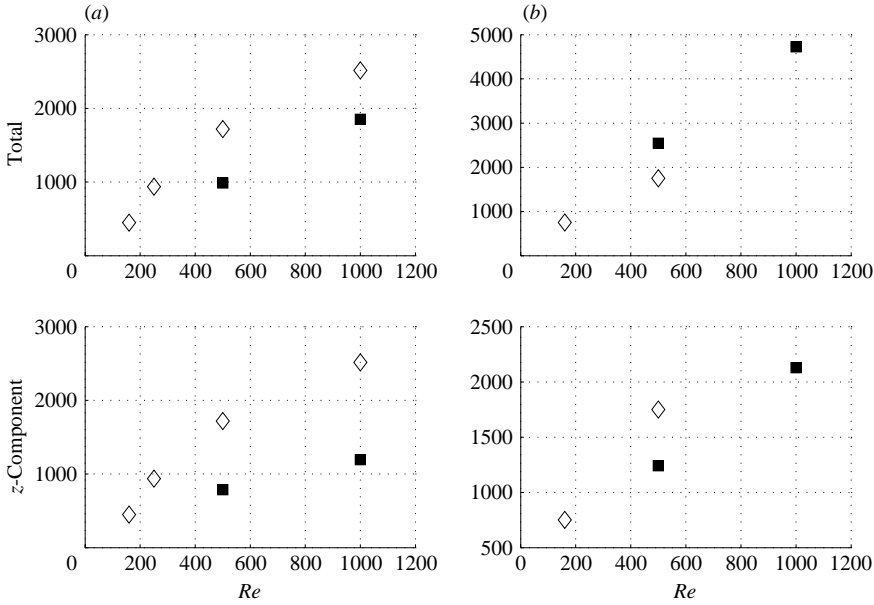


FIGURE 14. Variation of primary and total entrophy with Reynolds number and comparison between \diamond , two and \blacksquare , three dimensions for (a) $P/D = 3.5$, (b) 4.0.

where M is the number of recording points along the span. An overbar represents time averaging:

$$\overline{g(z, t)} = \frac{\sum_{k=1}^N g(z, t_k)}{N}, \quad (5.4)$$

where N is the number of discrete time samples of the signal. Spanwise fluctuations are represented with a prime ($'$):

$$g'(z, t) = g(z, t) - \langle g(z, t) \rangle. \quad (5.5)$$

Finally, for fluctuations in time we define:

$$\check{g}(z, t) = g(z, t) - \overline{g(z, t)}. \quad (5.6)$$

For the scope of the present paper and the way we have treated three-dimensionality so far, the intensity of the secondary instability is more relevant in quantifying three-dimensionality than the length scale of the spanwise fluctuations reflected in the *correlation length*. From here on, the ‘hat’ operation will denote Fourier transform to simplify notation.

The method used here involves calculating the energy of the spectrum of the spanwise fluctuations. Starting with the covariance between two stations z_i and z_j :

$$\tilde{R}(z_i, z_j) = \overline{\check{f}'(z_i, t)\check{f}'(z_j, t)} \quad (5.7)$$

the covariance function can be computed for each z_i simply by setting $z_j = z_i + \zeta$:

$$\tilde{R}(z_i, z_j) = R(z_i, z_i + \zeta) \equiv R(z_i, \zeta). \quad (5.8)$$

The last step can be implemented as a simple rearrangement of the elements of \tilde{R} , taking into account the periodicity imposed in the z -direction. Once $R(z_i, \zeta)$ is

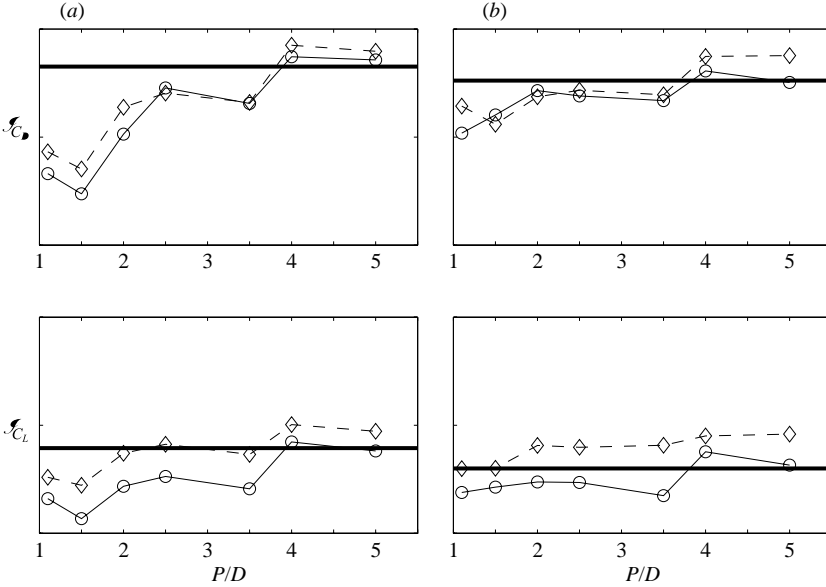


FIGURE 15. Effect of spacing on \mathcal{S}_3 based on fluctuations of the drag and lift forces on each cylinder, and comparison with the single cylinder for (a) $Re = 500$, (b) 1000. —○—, upstream cylinder; -◇-, downstream cylinder; —, single cylinder.

available, a Fourier transform in ζ (not z) is performed. This will be denoted by a double hat to emphasize that the transform is with respect to ζ . Squares of the absolute values of the coefficients form a spectrum for every different z_i . Then, an averaging in the spanwise direction and a summation yield the norm:

$$\mathcal{S} = \sum |\langle \widehat{\widehat{R}}(z_i, \zeta) \rangle|^2. \quad (5.9)$$

The method smooths (averages) in time first and along the span last, and relates to measuring the r.m.s. of the spanwise fluctuations (through Parseval's theorem).

The results are presented in figure 15. The plot is organized in columns of constant Reynolds number and rows corresponding to the time-histories used for the analysis (drag or lift). Each subplot contains results for both upstream and downstream cylinders as well as the single cylinder for comparison. The figure shows that the three-dimensionality in the force distribution along the span is higher on the downstream cylinder than the upstream. A sudden increase in \mathcal{S} as the spacing increases past the critical spacing can also be identified. The figure also shows that the energy of the spanwise fluctuations of the upstream cylinder is lower than that of the single cylinder throughout the reattachment regime. This supports the stabilization scenario proposed in this section. Another observation is that for the higher spacing examined ($P/D = 5.0$), the value coincides exactly with that corresponding to the single cylinder, showing that when the downstream cylinder is sufficiently downstream and well into the binary vortex regime the upstream cylinder behaves much like the single cylinder.

6. Summary

In the present work, two- and three-dimensional direct numerical simulations based on the spectral/hp element method have been performed to study the flow around

two stationary tandem cylinders in the laminar and early turbulent regimes. Good agreement was obtained with published experimental and two-dimensional numerical data. It was found that the two-dimensional results deviate increasingly from three-dimensional results with increasing Re , beyond a critical value for which there is onset of wake three-dimensionality. In the two-dimensional simulations, reattachment ceases for much smaller P/D values than in three-dimensional simulations. This causes large discrepancies in the forces and shedding frequencies for the range of spacings extending between the two- and three-dimensional predictions of the critical spacing. Systematic analysis showed that the differences in the prediction of the critical spacing between the two- and three-dimensional simulations for a given Reynolds number are related to the differences in the prediction of the formation length, or equivalently, the base pressure coefficient of a single cylinder.

Flow visualization showed an increase on the wake three-dimensionality as the cylinder spacing increased from values in the reattachment regime to values corresponding to the binary-vortex regime. A wake stabilization scenario was proposed suggesting that the presence of the downstream cylinder in spacing less than the critical value has a stabilizing effect on the wake. To support this scenario, we employed enstrophy integrals decomposed into a primary component associated with the primary vortex shedding and a secondary component involving vorticity components related to three-dimensional effects. Throughout the reattachment regime, all enstrophy components are below the corresponding ones for the single cylinder case. The situation is reversed for spacings in the binary-vortex regime.

The strength of three-dimensionality was alternatively quantified using the spanwise fluctuations of the forces on each cylinder in the tandem system. The results obtained are in agreement with the previous conclusions, and further verify the wake stabilization scenario. At the same time, they indicate increased intensity of three-dimensional fluctuations on the downstream cylinder compared to the upstream cylinder.

This work was supported by the Office of Naval Research. Computations were performed at the Naval Oceanographic Office (NAVOCEANO) Major Shared Resource Center (MSRC) and at NCSA University of Illinois at Urbana-Champaign.

Appendix. Convergence

A.1. Convergence of two-dimensional results

The mean drag coefficients of the upstream and downstream cylinders were used to study convergence along with the time average of the total enstrophy. See Papaioannou (2003) for extensive convergence tests by p-refinement, and several cases of comparisons between different meshes for a given spacing and Reynolds number.

Here the case of $P/D = 4.0$ and $Re = 500$ is selected for demonstration of convergence. Figure 16 shows convergence of the drag coefficients and the time average of the total enstrophy for this case. This case was chosen because it is towards the high end of the Reynolds numbers considered by the two-dimensional simulations. Furthermore, it is in the binary vortex regime where the vorticity is increased and there are steep gradients that have to be resolved. Prediction of the forces on the downstream cylinder, in particular, requires good resolution of the flow in the gap region. Figure 16 shows increased sensitivity of the drag coefficient for the downstream cylinder (C_{D2}). This is better demonstrated by the relative error. For the calculation

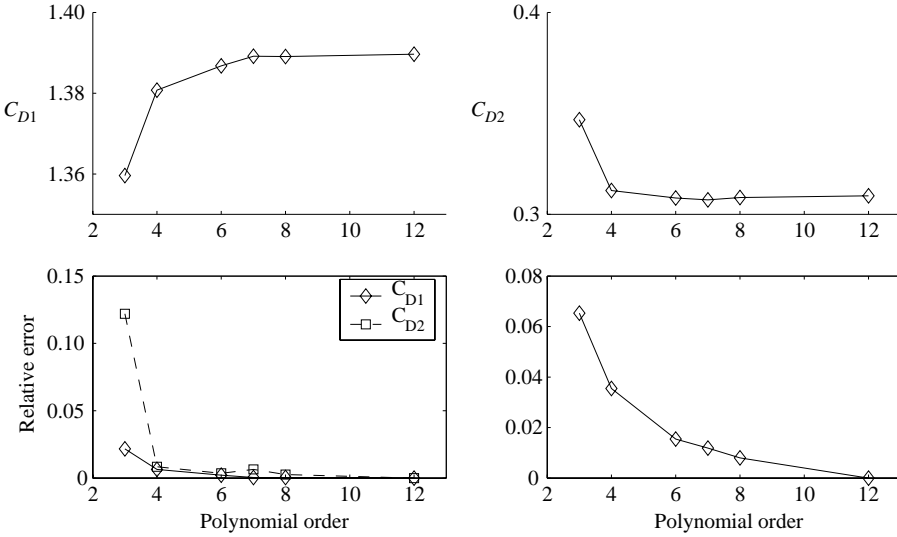


FIGURE 16. Demonstration of convergence for two-dimensional case $\{P/D=4.0, Re=500\}$. The drag coefficient of the upstream cylinder (C_{D1}) converges faster than that of the downstream cylinder (C_{D2}). Relative errors of C_{D1} , C_{D2} and total enstrophy are calculated based on the value of the corresponding quantity for the highest available polynomial order.

of the relative error, the result of the highest available polynomial order was used as reference:

$$\epsilon(p) = \left| \frac{C_{Di}(p) - C_{Di}(p_{max})}{C_{Di}(p_{max})} \right|, \tag{A 1}$$

where p denotes the polynomial order and p_{max} the maximum available p for the case presented, in this case $p_{max} = 12$. The relative error of the mean total enstrophy is defined similarly. The enstrophy integral is an appropriate norm to study convergence even in the mathematical sense. The enstrophy seems to converge slower than the drag coefficients. This can be explained in terms of the unstructured mesh used and shown in figure 17. The elements in the far wake are considerably larger in size than those in the near wake. The cylinder forces are not much influenced by under-resolution in the far wake. The enstrophy integral, however, captures them because it directly integrates over the whole domain. It should be noted that small fluctuations can also be attributed in the statistical error in calculating means of the forces and enstrophy. The highest polynomial order available in each case of spacing and Reynolds number was used for all the results presented in the text.

A.2. Convergence of three-dimensional results

The use of Fourier collocation in the spanwise direction alleviates the need for a fully three-dimensional mesh. Thus, the same meshes were used for the two- and three-dimensional simulations. Having ensured enough resolution in the transverse planes from the two-dimensional runs, the spanwise resolution had to be determined. In table 2, we compare the drag forces and shedding frequency between 32 and 64 planes in the spanwise direction. The columns of the compared quantities C_{D1} , C_{D2} and St are subdivided into two subcolumns one for each Re considered (500 and 1000). For each Re , there are two subcolumns corresponding to the spanwise resolutions 32 and 64. The rows of the table correspond to different cylinder spacing

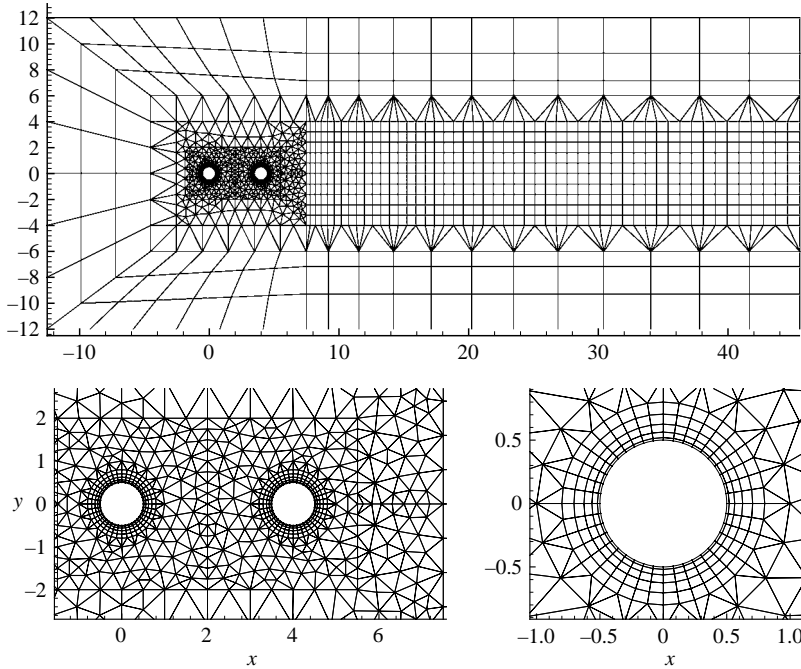


FIGURE 17. Computational mesh for case $P/D=4.0$. The final mesh is an assembly of mesh blocks. The mesh blocks add flexibility in the mesh generation process and lead to consistency among meshes corresponding to different spacings. For example, by reusing the outer mesh and changing only the mesh block $[-2.5, 7.5]D \times [-4.0, 4.0]D$. The O type mesh extending radially from $0.5D$ to $1.0D$ around each cylinder is also reusable.

Re	C_{D1}				C_{D2}				St			
	500		1000		500		1000		500		1000	
N_z	32	64	32	64	32	64	32	64	32	64	32	64
P/D												
S-A	1.196	1.154	NA	1.030	NA	NA	NA	NA	0.204	0.206	NA	0.216
1.1	1.088	NA	1.048	1.038	-0.250	NA	-0.308	-0.316	0.224	NA	0.244	0.252
1.5	1.016	1.016	1.002	1.004	-0.294	-0.294	-0.290	-0.310	0.154	0.154	0.162	0.168
2.0	1.016	1.016	0.986	0.988	-0.182	-0.180	-0.196	-0.174	0.156	0.154	0.168	0.172
2.5	0.958	NA	0.956	0.928	-0.142	NA	-0.096	-0.164	0.150	NA	0.154	0.158
3.5	0.882	0.894	NA	0.856	-0.144	-0.126	NA	-0.158	0.144	0.144	NA	0.156
5.0	1.078	1.082	0.946	0.956	0.584	0.552	0.604	0.582	0.190	0.192	0.204	0.190

TABLE 2. Comparison of drag forces on upstream and downstream cylinders, as well as shedding frequencies for spanwise resolutions $N_z=32$ and $N_z=64$. For each quantity, C_{D1} , C_{D2} and St , the two examined Reynolds numbers are shown; and for each Re , the two available resolutions and the results they yield for different spacings (P/D) and the single-cylinder case are given.

P/D , and one to the single, cylinder case (S-A). Convergence is demonstrated when two consecutive numbers corresponding to the same P/D and Re , but different N_z , have small relative error. For illustration, consider the case $P/D=5.0$ for $Re=500$.

The relative error in the calculation of the upstream cylinder drag coefficient C_{D1} is $|1.082 - 1.078|/1.082 = 0.37\%$. For the same case and the downstream cylinder drag coefficient C_{D2} , the relative error is $|0.552 - 0.584|/0.552 = 5.8\%$. To find the relative error, we divide by the higher-resolution case ($N_z = 64$) result, because it is expected to be closer to the actual value.

For the drag coefficient of the upstream cylinder C_{D1} at $Re = 500$, the relative error from 32 to 64 z -planes is less than 1.5% with several cases in the reattachment regime giving a four significant digits agreement. At $Re = 10^3$, the relative error reaches 3% in one case and is below 1.2% for the rest available with two cases having agreement within 0.2%.

As we would expect, the drag coefficient of the downstream cylinder C_{D2} is more sensitive to the spanwise resolution owing to the three-dimensionality that has developed in the gap region. The discrepancies between the results of 32 planes and 64 planes are relatively small ($\approx 2\text{--}3\%$) in the early reattachment regime, but reach about 13–14% as the spacing increases towards the critical spacing. For the binary vortex regime case provided in table 2 ($P/D = 5.0$) the agreement is within 6% error.

The maximum available resolution result of each case was used for all further analysis.

REFERENCES

- BARKLEY, D. & HENDERSON, R. 1996 Three-dimensional Floquet stability analysis of the wake of a circular cylinder. *J. Fluid Mech.* **322**, 215–241.
- BEARMAN, P. W. 1965 Investigation of the flow behind a two-dimensional model with a blunt trailing edge and fitted with splitter plates. *J. Fluid Mech.* **21**, 241–255.
- BLOOR, M. S. 1964 The transition to turbulence in the wake of a circular cylinder. *J. Fluid Mech.* **19**, 290–304.
- BLOOR, M. S. & GERRARD, J. H. 1966 Measurements on turbulent vortices in a circular cylinder. *Proc. R. Soc. Lond. A* **294**, 319–342.
- EVANGELINOS, C. & KARNIADAKIS, G. E. 1999 Dynamics and flow structures in the turbulent wake of rigid and flexible cylinders subject to vortex-induced vibrations. *J. Fluid Mech.* **400**, 91–124.
- GERRARD, J. H. 1966 The mechanics of the formation region of vortices behind bluff bodies. *J. Fluid Mech.* **25**, 401–413.
- HENDERSON, R. & BARKLEY, D. 1996 Secondary instability in the wake of a circular cylinder. *Phys. Fluids* **8**, 1683–1685.
- HENDERSON, R. & KARNIADAKIS, G. E. 1995 Unstructured spectral element methods for simulation of turbulent flows. *J. Comput. Phys.* **122**, 191–217.
- HOVER, F. S. & TRIANTAFYLLOU, M. S. 2001 Galloping response of a cylinder with upstream wake interference. *J. Fluids Struct.* **15**, 503–512.
- IGARASHI, T. 1981 Characteristics of the flow around two circular cylinders arranged in tandem, 1st report. *Bull. JSME B27(233)*, 2380–2387.
- JESTER, W. & KALLINDERIS, Y. 2003 Numerical study of incompressible flow about fixed cylinder pairs. *J. Fluids Struct.* **17**, 561–577.
- KARNIADAKIS, G. E., ISRAELI, M. & ORSZAG, S. A. 1991 High-order splitting methods for the incompressible Navier–Stokes equations. *J. Comput. Phys.* **97**, 414–443.
- KARNIADAKIS, G. E. & SHERWIN, S. J. 1999 *Spectral/hp Element Methods for CFD*. Oxford University Press.
- KARNIADAKIS, G. E. & TRIANTAFYLLOU, G. S. 1992 Three-dimensional dynamics and transition to turbulence in the wake of bluff bodies. *J. Fluid Mech.* **238**, 1–30.
- LIN, J. C., TOWFIGHI, J. & ROCKWELL, D. 1995 Instantaneous structure of the near-wake of a circular cylinder: on the effect of Reynolds number. *J. Fluids Struct.* **9**, 409–418.

- LJUNGKRONA, L., NORBERG, C. & SUNDEN, B. 1991 Free-stream turbulence and tube spacing effects on surface pressure fluctuations for two tubes in an in-line arrangement. *J. Fluids Struct.* **5**, 701–727.
- MENEIGHINI, J. R., SALTARA, F., SIQUEIRA, C. L. R. & FERRARI JR, J. A. 2001 Numerical simulation of flow interference between two circular cylinders in tandem and side-by-side arrangements. *J. Fluids Struct.* **15**, 327–350.
- MITTAL, S., KUMAR, V. & RAGHUVANSHI, A. 1997 Unsteady incompressible flows past two cylinders in tandem and staggered arrangements. *Intl J. Numer. Meth. Fluids* **25**, 1315–1344.
- NOAK, B. R. & ECKELMANN, H. 1994 A global stability analysis of the steady and periodic cylinder wake. *J. Fluid Mech.* **270**, 297–330.
- NORBERG, C. 1987 Turbulence and Reynolds number effects on the flow and fluid forces on a single cylinder in cross flow. *J. Fluids Struct.* **1**, 337–357.
- NORBERG, C. 1994 An experimental investigation of the flow around a circular cylinder: Influence of aspect ratio. *J. Fluid Mech.* **258**, 287–316.
- NORBERG, C. 1998 LDV-measurements in the near wake of a circular cylinder. In *Advances in understanding of Bluff Body Wakes and Flow-Induced Vibration* (ed. C. H. K. Williamson & P. W. Bearman), pp. 1–12. (FEDSM98-5202). ASME, New York.
- OKA, S., KOSTIC, Z. G. & SIKMANOVIC, S. 1972 Investigation of the heat transfer process in tube banks in cross flow. *Intl Seminar on Recent Development in Heat Exchangers, Trogir, Yugoslavia*.
- OKAJIMA, A. 1979 Flows around tandem circular cylinders at very high Reynolds numbers. *Bull. JSME* **22**, 504–511.
- PAPAIOANNOU, G. 2003 A numerical study of flow-structure interactions with application to flow past a pair of cylinders. PhD thesis, Department of Ocean Engineering, Massachusetts Institute of Technology.
- PERSILLON, H. & BRAZA, M. 1998 Physical analysis of the transition to turbulence in the wake of a circular cylinder by three-dimensional Navier–Stokes simulation. *J. Fluid Mech.* **365**, 23–88.
- ROSHKO, A. 1954 On the development of turbulent wakes from vortex streets. *NACA Rep.* 1191.
- ROSHKO, A. 1961 Experiments on the flow past a circular cylinder at very high Reynolds number. *J. Fluid Mech.* **10**, 345–356.
- SHARMAN, B., LIEN, F. S., DAVIDSON, L. & NORBERG, C. 2005 Numerical predictions of low Reynolds number flows over two tandem circular cylinders. *Intl J. Numer. Meth. Fluids* **47**, 423–447.
- SLAOUTI, A. & STANSBY, P. K. 1992 Flow around two circular cylinders by the random-vortex method. *J. Fluids Struct.* **6**, 641–670.
- SUMNER, D., PRICE, S. J. & PAIDOUSSIS, M. P. 1999 Tandem cylinders in impulsively started flow. *J. Fluids Struct.* **13**, 955–965.
- SUMNER, D., RICHARDS, M. D. & AKOSILE, O. O. 2005 Two staggered circular cylinders of equal diameter in cross-flow. *J. Fluids Struct.* **20**, 255–276.
- TANIDA Y., OKAJIMA, A. & WATANABE, Y. 1973 Stability of a circular-cylinder oscillating in uniform flow or in a wake. *J. Fluid Mech.* **61**, 769–784.
- WARBURTON, T. 1998 Spectral/hp element methods on polymorphic multi-domains: algorithms and applications. PhD thesis, Division of Applied Mathematics, Brown University.
- WILLIAMSON, C. H. K. 1988 The existence of two stages in the transition to three-dimensionality of a cylinder wake. *Phys. Fluids* **31**, 3165–3168.
- WILLIAMSON, C. H. K. 1996 Vortex dynamics in the cylinder wake. *Annu. Rev. Fluid Mech.* **28**, 477–539.
- WILLIAMSON, C. H. K. & ROSHKO, A. 1990 Measurements of base pressure in the wake of a cylinder at low Reynolds numbers. *Z. Flugwiss. Weltraumforschung* **14**, 38–46.
- XU, G. & ZHOU, Y. 2004 Strouhal numbers in the wake of two inline cylinders. *Exps. Fluids* **37**, 248–256.
- ZDRAVKOVICH, M. M. 1977 Review of flow interference between two circular cylinders in various arrangements. *J. Fluids Engng* **99**, 618–633.
- ZDRAVKOVICH, M. M. 1984 Classification of flow-induced oscillations of two parallel circular cylinders in various arrangements. *Symp. on Flow-Induced Vibrations* vol. 2, pp. 1–18.
- ZDRAVKOVICH, M. M. 1987 The effect of interference between circular cylinders in cross flow. *J. Fluids Struct.* **1**, 239–261.